Electron Transfer through 3D Monolayers on Au_{25} Clusters

Sabrina Antonello,[†] Giorgio Arrigoni,[‡] Tiziano Dainese,[†] Marco De Nardi,[†] Giulia Parisio,[†] Lorena Perotti,[†] Alice René,[†] Alfonso Venzo,[†,§] and Flavio Maran[†,*]

[†]Department of Chemistry, and [§]IENI-CNR c/o Department of Chemistry, University of Padova, via Marzolo 1, 35131 Padova, Italy, and [‡]Department of Biomedical Sciences, University of Padova, Viale G. Colombo 3, 35121 Padova, Italy

ABSTRACT The monolayer protecting small gold nanoparticles (monolayer-protected clusters, MPCs) is generally represented as the 3D equivalent of 2D self-assembled monolayers (SAMs) on extended gold surfaces. However, despite the growing relevance of MPCs in important applied areas, such as catalysis and nanomedicine, our knowledge of the structure of 3D SAMs in solution is still extremely limited. We prepared a large series of monodisperse $Au_{25}(SC_nH_{2n+1})_{18}$ clusters ($n = 2, 4, 6, 8, 10, 12, 14, 16, 18$) and studied how electrons tunnel through these monolayers. Electron transfer results, nicely supported by ^1H NMR spectroscopy, IR absorption spectroscopy, and molecular dynamics results, show that there is a critical ligand length marking the transition between short ligands, which form a quite fluid monolayer structure, and longer alkyl chains, which self-organize into bundles. At variance with the truly protecting 2D SAMs, efficient electronic communication of the Au_{25} core with the outer environment is thus possible even for long alkyl chains. These conclusions provide a different picture of how an ultrasmall gold core talks with the environment through/with its protecting but not-so-shielding monolayer.

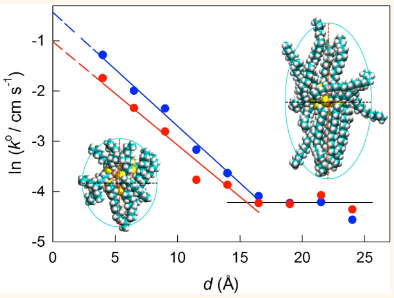

KEYWORDS: gold nanoclusters · $Au_{25}(SR)_{18}$ · electron transfer · molecular electrochemistry · self-assembled monolayers

By far, $Au_{25}(SR)_{18}$ is the most representative case of a stable monolayer-protected cluster (MPC) possessing a metal core sufficiently small (1 nm) to cause the system to display a distinct molecule-like behavior.[1] MPC monolayers are generally depicted as capping shields protecting the core from aggregation and a way to display functional groups for possible applications.[2−5] These monolayers are, in fact, complex 3D nanosystems. The structure of $Au_{25}(SC_2H_4Ph)_{18}$ shows a 13-atom icosahedral inner Au core surrounded by 6 $Au_2(SC_2H_4Ph)_3$ staple-like semirings.[6−8] Staple-like bonding motifs are also present in larger clusters.[9−12] Interestingly, similar thiolate-Au features are also found in self-assembled monolayers (SAMs) on extended gold surfaces (2D SAMs).[13] That the same Au−S binding motifs can be found in both 2D and 3D SAMs points to very similar interactions and mutual stabilization of surface Au atoms and thiolated species.[14,15] However, whereas in 2D SAMs molecular adsorbates primarily interact *via* interchain van der Waals forces allowing formation of regular domains of parallel molecules,[16] it is not clear if similar interactions are equally important or even present at all in the monolayers of molecule-like MPCs. For example, whereas 2D SAMs are sufficiently compact to hamper penetration of molecular probes (so-called blocking effect: reduction or oxidation of molecular probes present in solution is hampered),[17] electrochemistry provided evidence that MPC monolayers allow some solvent/electrolyte penetration.[18,19] The possible structure of 3D SAMs has been discussed on the basis of earlier seminal IR absorption, solid-state NMR, and molecular dynamics (MD) studies of larger MPCs.[20−24] Concerning molecule-like MPCs, however, and despite their interest as catalytic systems in redox processes, the monolayer structure in solution is still undefined. Because of its well-defined composition[25,26] and unique electrochemical, optical, and magnetic features,[27−29] the atomically monodisperse $Au_{25}(SR)_{18}$ cluster provides an ideal benchmark for addressing this issue through the study of reactions occurring at, in, or through a 3D SAM or, to better say, the complex interfacial region between the gold core and the surrounding medium.

A reaction particularly appealing to assess the structure of MPCs' monolayers is

* Address correspondence to flavio.maran@unipd.it.

Received for review December 19, 2013 and accepted January 17, 2014.

10.1021/nn406504k

electron transfer (ET). ET is an extremely important reaction ubiquitous to a variety of biochemical and chemical areas,[30,31] including redox catalysis with ultrasmall Au nanoparticles.[3,5,19,32] Our understanding of the rate and mechanisms of long-range ETs through molecular bridges strongly relies on the outcome of studies carried out with 2D SAMs.[17] These and related studies allowed establishing distance dependence descriptors for a number of molecular bridges.[30,33,34] According to the superexchange mechanism,[31,34] the ET rate constant (k_{ET}) depends exponentially on the donor–acceptor distance (r_{DA}) *via* eq 1

$$k_{ET} = k_{ET}^{0}\exp(-\beta r_{DA}) \qquad (1)$$

where the parameter β describes the falloff of the electron tunneling rate through the specific bridge and k_{ET}^{0} is the ET rate constant at contact distance. For an alkyl chain in its all-*trans* conformation, which is the most efficient conformation for mediating ETs,[34] the distance "ruler" is β = 0.8–1.0 Å^{-1}.[30,33,34] This important insight comes from studies of well-organized 2D SAMs,[17] metal–bridge–metal junctions,[33] and rigid donor–bridge–acceptor systems.[34] Can we now reverse the concept and use ET rulers as probes of the solution-phase structure of the otherwise elusive 3D monolayers of molecule-like MPCs such as $Au_{25}(SR)_{18}$? To which extent can the general picture valid for 2D SAMs be extended to the monolayer of 3D SAMs such as those formed on Au_{25} clusters?

Here we address these issues by studying the kinetics of electron tunneling through the monolayer of $Au_{25}(SR)_{18}$ clusters. By using a large series of alkanethiols, ranging from the shortest (C2) to the longest (C18) ligand ever used for such clusters, we prepared a homogeneous family of monodisperse $Au_{25}(SC_nH_{2n+1})_{18}$ clusters, with n = 2, 4, 6, 8, 10, 12, 14, 16, 18. Our study provides the first analysis of the distance effect on the ET rate through 3D monolayers assembled on a gold cluster. Unexpected heterogeneous ET rates, together with converging results obtained by solution-phase ^{1}H NMR spectroscopy, IR absorption spectroscopy, and MD calculations, provide compelling evidence that while for the shorter ligands the monolayer can be described by a fluid structure of folded chains, longer alkyl chains self-organize into bundles. At variance with 2D SAMs, which provide efficient shields of the underlying gold surface, efficient electronic communication of the Au_{25} core with the outer environment is thus possible even for long alkyl chains.

RESULTS AND DISCUSSION

We prepared a series of $Au_{25}(SC_nH_{2n+1})_{18}$ clusters in which n = 2, 4, 6, 8, 10, 12, 14, 16, 18. The syntheses were carried out in tetrahydrofuran, similarly to that described for $Au_{25}(SC_2H_4Ph)_{18}$.[28] Briefly, a solution of tetrachloroauric acid in the presence of 1.1 equiv of tetraoctylammonium bromide is allowed to react with the appropriate alkanethiol until the initially red solution becomes colorless, which is indicative of quantitative reduction of Au(III) to form reactive Au(I)-thiolate species. Addition of an aqueous solution of sodium borohydride causes rapid reduction to Au(0), with formation of a black solution. After typically 3 days under stirring, the clusters are separated from the reaction solution. As a final step, the Au_{25} clusters, which originally form in the anionic state,[25,26] are quantitatively oxidized to their stable neutral form; we found that silica gel column chromatography performs particularly well to obtain $Au_{25}(SC_nH_{2n+1})_{18}^{0}$ in a very pure form. We will now denote the clusters simply as $Au_{25}(SCn)_{18}$, where n is the number of carbon atoms.

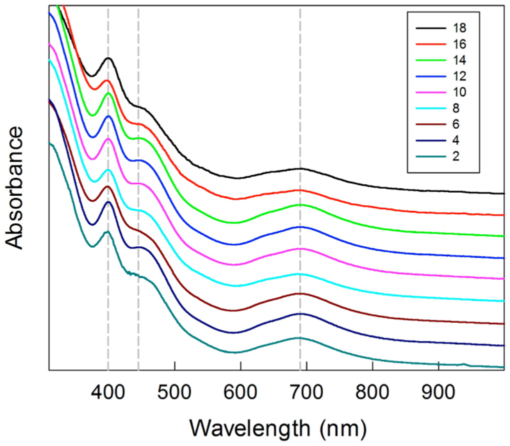

Figure 1. Comparison of the UV–vis absorption spectra of $Au_{25}(SCn)_{18}^{0}$. The measurements were carried out in dichloromethane (C2–C14) or benzene (C16, C18) at 25 °C. For clarity, the spectra have been vertically shifted. Dashed lines mark the main spectral features.

The UV–vis spectra of $Au_{25}(SCn)_{18}^{0}$ (Figure 1) show the expected features of monolayer-protected Au_{25} clusters in their 0 charge state,[8,28] such as the presence of a peak at 400 nm, a shoulder at *ca.* 445 nm, and a broad peak at 690 nm. We note that the features corresponding to the −1 or the +1 charge state, the latter possibly obtained by further oxidation of $Au_{25}(SCn)_{18}^{0}$, are distinctly different.[28] For n = 2–14, the average molar extinction coefficient at 400 nm is 5.5 × 10^4 M^{-1} cm^{-1}, that is, essentially the same as that of $Au_{25}(SC_2H_4Ph)_{18}$, 5.38 × 10^4 M^{-1} cm^{-1}, which nicely points to the optical behavior of $Au_{25}(SR)_{18}$ clusters (SR = generic thiolated ligand) as virtually only determined by the structure of the gold core. We found that for the longer ligands (n = 14–18), the peak at 400 nm increases while the band at 690 nm becomes less pronounced. This behavior is attributed to aggregation phenomena in solution, and as a matter of fact, when these solutions are sonicated (ultrasounds), the spectra become much more similar to those of the other clusters: the spectra of Figure 1 (n = 14–18) were obtained after sonication. Benzene solubilizes the C14,

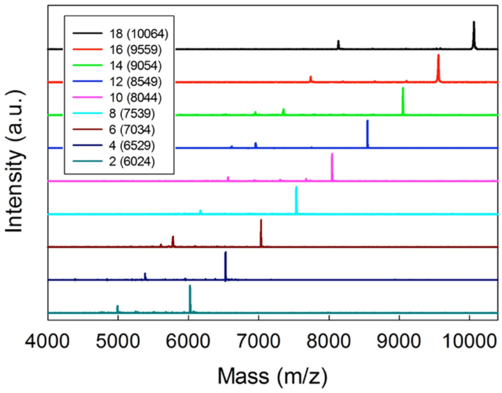

Figure 2. MALDI-TOF mass spectra of $Au_{25}(SCn)_{18}^0$. For clarity, the spectra have been vertically shifted. The legend shows the MPCs' molecular weights.

C16, and C18 MPCs in an amount of time (~3, 10, and 15 min, respectively) shorter than any other solvent tested.

The composition and monodispersity of each $Au_{25}(SCn)_{18}$ cluster were assessed by matrix-assisted laser desorption ionization time-of-flight (MALDI-TOF) mass spectrometry, a particularly effective technique for this class of clusters.[35] Figure 2 shows that each spectrum displays the peak corresponding to the parent cluster and some evidence of the main fragmentation pattern. Although fragmentation can be minimized to virtually nothing by decreasing the intensity of the laser power as much as possible, it is nonetheless useful because close inspection of the spectra obtained with a slightly larger laser energy reveals that the clusters undergo the same fragmentation pattern already noted for $Au_{25}(SC_2H_4Ph)_{18}$, that is, stepwise loss of AuSR fragments to form $Au_{21}(SR)_{14}$. The parent peaks have masses perfectly matching the calculated molecular weights. Noteworthy, this is also true for the C14, C16, and C18 MPCs, despite their pronounced sonication-dependent UV–vis behavior. Overall, MALDI-TOF thus provides compelling evidence that all $Au_{25}(SCn)_{18}$ investigated share the same formula and features.

The ^1H NMR behavior of the ligands capping Au_{25} clusters is very sensitive to the specific ligand type.[1,28] The 18 ligands split into a group of 6 outer and 12 inner ligands: we here define as outer the ligands in which S is bound to two stellated Au atoms and as inner those in which one of the two S–Au bonds involves the 13-atom icosahedral Au core (Figure 3A). The ^1H NMR measurements were carried out in benzene-d_6. The spectra revealed the same general features of $Au_{25}(SC_2H_4Ph)_{18}$, for which we could solve the details of each resonance of the two ligand groups as a function of the core charge state.[28] $Au_{25}(SCn)_{18}^0$ is paramagnetic: for the 12 inner ligands, the resonance of the methylene group closer to the sulfur atom, $(\alpha\text{-}CH_2)_{in}$, is particularly sensitive to the paramagnetic character of the cluster and is found at very large chemical shift (δ) values. This resonance is barely observable at 25 °C but develops into a nicely detectable peak at higher temperatures (for example, see Figure S1 of Supporting Information): for $n = 4–18$, $\delta = 22.5 \pm 0.2$ at 65 °C. The other features of the ^1H NMR spectra are also very similar. All resonances, which were assigned by analysis of homo- and heteronuclear 2D correlation spectra, occur at δ values that reflect the specific type of ligand (with integrals in a 2:1 ratio, in agreement with 12 inner *vs* 6 outer ligands) and the position of methylene with respect to sulfur (α, β, γ, and so on). The peaks of the methylene groups closer to the Au core occur at $(\alpha\text{-}CH_2)_{out}$, 5.06–5.20 ppm; $(\beta\text{-}CH_2)_{in}$, 3.48–3.61 ppm; $(\gamma\text{-}CH_2)_{in}$, 2.56–2.67 ppm; $(\delta\text{-}CH_2)_{in}$, 1.96–2.10 ppm; $(\beta\text{-}CH_2)_{out}$, 1.74–1.92 ppm; $(\gamma\text{-}CH_2)_{out}$, 1.57–1.71 ppm. Figure 3B shows the spectral regions pertaining to $(\alpha\text{-}CH_2)_{out}$ and $(\beta\text{-}CH_2)_{in}$ (for the full spectra, see Figure S2). Comparison of the spectra shows the interesting pattern that the $(\alpha\text{-}CH_2)_{out}$ and $(\beta\text{-}CH_2)_{in}$ resonances do not appreciably change as one goes from $n = 18$ to $n = 10$, but when the chain becomes shorter, δ distinctly decreases (upfield shift). The other methylene resonances display a very similar trend, once again with C10 as the turning point at which δ starts shifting to lower values. These results indicate that for C10 and longer chains there is no significant difference in terms of the chemical environment experienced by the above methylene groups. A plausible hypothesis is thus that

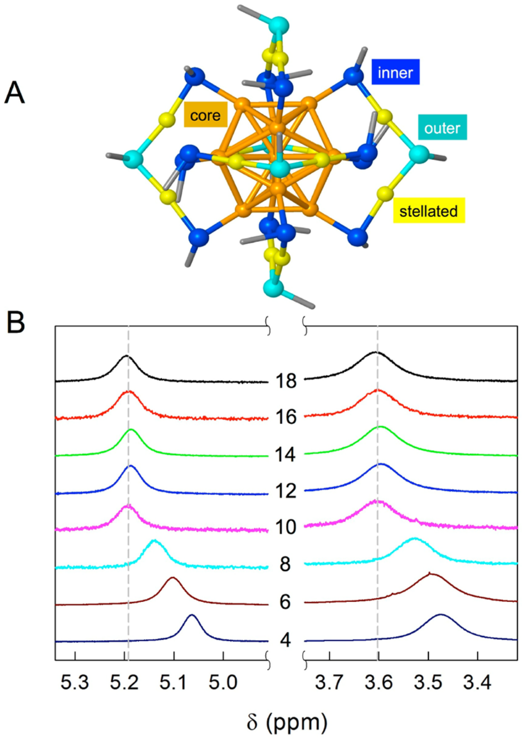

Figure 3. (A) Main structural features of $Au_{25}(SR)_{18}^0$ (coordinates from ref 8): core Au atoms (dark yellow), stellated Au atoms (light yellow), inner ligand S atoms (blue), and outer ligand S atoms (light blue). (B) ^1H NMR spectra of monodisperse $Au_{25}(SCn)_{18}^0$ in benzene-d_6 at 25 °C: the spectral zones show the $(\alpha\text{-}CH_2)_{out}$ (left) and $(\beta\text{-}CH_2)_{in}$ (right) resonances. Dashed lines mark the average chemical shifts calculated for C10–C18.

the longer ligands interact with each other in a way that is virtually unaffected by further elongation of the chain. Shorter chains, on the other hand, have more conformational freedom and are thus more extensively surrounded by benzene molecules, a solvent known to cause resonances to undergo an upfield shift.[36]

IR absorption spectroscopy has proved to be a valuable tool for studying the structure of alkanethiolate SAMs on flat gold.[16] Studies with alkanethiolate-protected Au nanoparticles larger than Au_{25} MPCs[20−22] showed that compared to conventional 2D SAMs the average surface curvature of MPCs is such to make the monolayer periphery relatively mobile. In this framework, the $Au_{25}(SCn)_{18}$ family provides a new situation for both the smaller (and totally controlled) core dimension and the presence of different binding sites (not facets, as for larger clusters) for the thiolates. For both symmetric ($d+$) and antisymmetric ($d-$) CH_2 stretching modes, which are particularly diagnostic for obtaining information about the conformation of alkyl chains, we found that as *n* increases up to 10 the frequencies undergo a progressive red shift (Figures S3−S5) similar to that observed for the free alkanethiols. For longer ligands, however, the frequency initially increases and then drops to values similar to those measured for 2D SAMs[37] and larger MPCs,[38] which are typical of extended all-*trans* conformation. Overall, the IR results thus concur with the NMR evidence in indicating a structural transition as one goes from shorter to longer ligands.

Over the last 25 years, the rate of electron tunneling through a variety of molecular bridges has been established.[17,30,33,34] Here the concept will be reversed in the sense that ET will be used as an indicator of apparent deviations from the distance dependence expected for alkyl chains. Because ET is sensitive to the distance separating the exchanging centers and the nature of the molecular bridge, to gain further insights into the structure of $Au_{25}(SCn)_{18}$ monolayers, we studied the effect of the ligand length on electrode kinetics. Au_{25} clusters can be conveniently charged by stepwise electrochemical reduction or oxidation.[18] However, whereas the 0/−1 and +1/0 redox couples display a chemically reversible voltammetric behavior at all potential scan rates (*v*), further reduction or oxidation generates species with limited lifetimes.[19,29] We thus focused on the 0/−1 and +1/0 redox couples. The kinetics of the first reduction (R1) and oxidation steps (O1) of $Au_{25}(SCn)_{18}{}^0$ was studied by cyclic voltammetry (CV) in dichloromethane (DCM) containing 0.1 M tetra-*n*-butylammonium hexafluorophosphate (TBAH). Based on the above evidence, the experiments concerning the C14, C16, and C18 MPCs were carried out after sonication of the corresponding solutions for the appropriate time (as assessed by UV−vis control experiments).

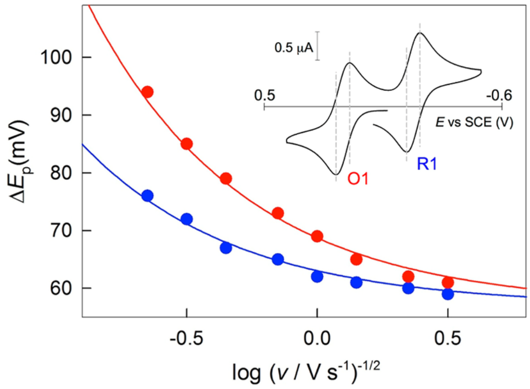

Figure 4. Scan rate dependence of ΔE_p for R1 (blue) and O1 (red): 0.51 mM $Au_{25}(SC4)_{18}{}^0$ in DCM/0.1 M TBAH on the glassy carbon electrode at 25 °C. The lines are the best fit of the Nicholson curve[39] to the data. The inset shows a typical CV (positive initial scan direction) with vertical lines evidencing ΔE_p.

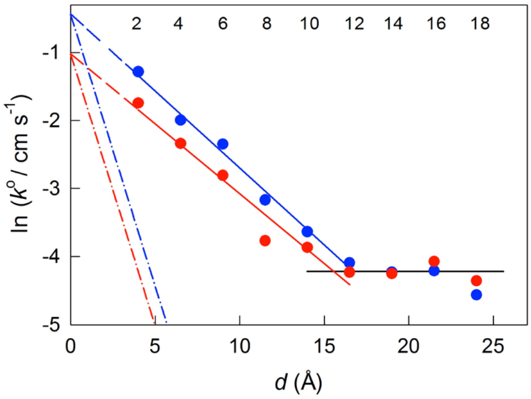

Figure 5. Distance effect on the heterogeneous ET rate constants for R1 (blue) and O1 (red). The distance *d* corresponds to fully extended conformations. Uncertainty in ln k^0 values is 0.05−0.1. Linear regressions correspond to β = 0.23 (R1) and 0.21 $Å^{-1}$ (O1). The two dash-dot lines and the horizontal line correspond to β = 0.8 and 0 $Å^{-1}$, respectively.

At low *v* values, both R1 and O1 peaks display the typical peak-to-peak separation (ΔE_p) of ∼59 mV expected for a reversible one-electron process at 25 °C.[39] On the other hand, when the time scale of the voltammetric experiment is made small, ΔE_p increases, which indicates that the heterogeneous ET becomes quasi-reversible. This is illustrated in the typical plots of Figure 4 for both peaks R1 and O1. The ΔE_p dependence on *v* can be quantitatively analyzed[39] to obtain the standard heterogeneous ET rate constant k^0, which is the ET rate constant measured at the formal potential (E^0). Because we started from the neutral cluster, the R1 and O1 processes could be studied independently by running the CV scan toward negative or positive potentials, respectively, starting from the equilibrium potential of $Au_{25}(SCn)_{18}{}^0$. The k^0 results were confirmed by digital simulation of the CV curves. Figure 5 illustrates the outcome of these measurements and calculations. The k^0 values are plotted as a function of the distance *d* between the surface gold atoms and the solution-side end of the ligands, assuming a fully extended conformation. For both R1 and O1, the plots reveal three important aspects: (i) for ligands with short to moderately long chains ($n = 2-12$), the falloff of the ET rate with distance is linear; (ii) the corresponding β values (cf. eq 1) are 0.23 and 0.21 $Å^{-1}$, in sharp contrast even to the minimum value of β, 0.8 $Å^{-1}$, determined for saturated sp^3 carbon chains in solution or 2D SAMs; (iii) for longer ligands (C12−C18), a sizable change in slope is observed, and in fact, the ET rate becomes virtually independent of the ligand length.

Former ET evidence showed that through-bond coupling is maximized (smaller β value) when alkyl chains adopt an all-*trans* conformation, whereas introduction of *cis* kinks decrease the ET rate.[34] Concerning C2−C12, the observed very low β values cannot thus indicate that a somehow more efficient conformation is attained. Instead, these apparent β factors point to electron tunneling as occurring at an average distance equivalent to approximately one-fourth of the fully extended lengths of the ligands. This implies that the monolayer chains are substantially bent with respect to the electrode−gold core separation. The ET rates and mild distance dependencies thus provide smoking-gun evidence that 3D monolayers of molecule-like Au clusters cannot be depicted as a more or less regular arrangement of ligands pointing outward, as often assumed and illustrated. In this context, it is worth mentioning that heterogeneous ET rates measured for larger MPCs (displaying quantized charging behavior)[2] yielded a β value of 0.41 $Å^{-1}$;[40] with all due cautions associated with the polydisperse MPCs employed, comparison with our results would point, not quite unexpectedly, to a core-size-dependent ET β factor.

What happens for the longer chains is also very interesting. For the same reasons already described, the virtual independence of the ET rate on the ligand length is only apparent. In fact, the ET can be taken as a sensitive probe of the new situation occurring to the monolayers composed by long ligands. Generally speaking, ET rate constants are the time average of electron tunneling events occurring in a range of rate-significant donor−acceptor distances and, for intramolecular ETs, orientations. Because of this, even subtle differences between intermolecular and intramolecular ET rates can be detected.[41] In principle, heterogeneous ETs to/from symmetrically protected MPCs should provide the very special case of bimolecular ETs occurring through a molecular spacer, like in intramolecular ETs, but with rates independent of orientation. In fact, our results point to an orientation-dependent process and, specifically, that the average monolayer thickness is not constant around the MPC. For chains with a length equal or longer than C12, there are MPC's orientations for which ET occurs at a distance that virtually does not change with ligand length. These orientations correspond to the MPC with its thinner sides closer to the electrode surface and are those providing the dominant contributions to the observed ET rate constant. The anomalous dependence of the heterogeneous ET rate on distance illustrated in Figure 5 thus detects and amplifies those chain-length-dependent monolayer features inferred from the NMR and IR results. We can thus conclude that while on the small surface of Au_{25} clusters the shorter thiolated ligands are quite mobile and the interaction among chains is not significant, longer ligands self-arrange in bundles because of cooperative van der Waals interactions. Since the Au core is small, once the chains start interacting, they can only do it along preferred orientations. This implies that the ligands leave the Au core much less shielded than expected on the basis of a fully extended conformation.

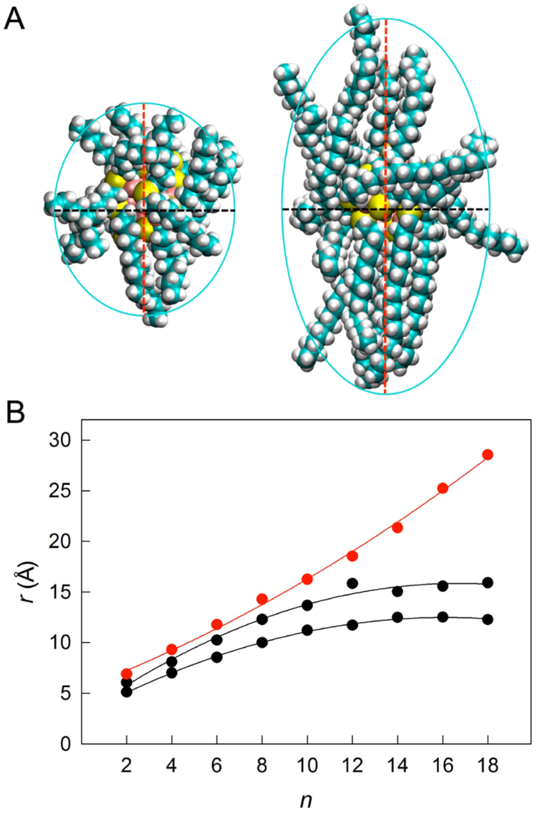

Figure 6. (A) Representative snapshots from the MD trajectories of approximately spherical C10 (left) and elongated C18 MPCs (right), in benzene at 300 K. Dashed lines indicate the long (red) and one of the perpendicular (black) axes. (B) Dependence of the semiaxis lengths *a* (red) and *b* and *c* (black) on the number of carbon atoms in the chain.

To shed further light onto this intriguing and fascinating issue, we performed MD calculations of the clusters' monolayers in benzene. The components of the inertia tensor **I** are a measure of the size of $Au_{25}(SCn)_{18}$ along its three main axes. Whereas spherical particles are characterized by isotropic tensors, for anisotropic particles, asymmetry and relative magnitude of the principal components determine the particle's shape. The components of the tensor **I** monotonically increase with the length of chains but with different dependencies (Figure S6). Figure 6A illustrates that MPCs capped by not-too-long alkanethiolates are indeed nearly spherical, which corresponds to similar components of **I**. In particular, the MD trajectories show that these chains independently fluctuate in the solvent, without displaying any orientation preference. For longer chains, on the other hand, one of the components of **I** is significantly smaller (corresponding to the longest axis), which imparts the MPCs an elongated shape: this is because the chains tend to attain an extended conformation and assemble by forming two bundles on opposite sides of the gold core. These snapshots suggest that the MPCs' shape can be satisfactorily described with ellipsoids. In Figure 6B, the lengths *a*, *b*, and *c* of the three semiaxes, obtained from the components of the diagonalized inertia tensor, are plotted as a function of *n*. While *b* and *c* increase and then level off for $n \sim 12$, semiaxis *a* monotonically increases and displays an even slightly steeper dependence on *n* beyond the C12 critical length. Addition of further methylene units to the C12 chain thus induces elongation only in the direction *a*, with chains progressively assuming a more extended conformation.

CONCLUSIONS

By using a large series of alkanethiols, we prepared a homogeneous family of monodisperse Au_{25} clusters. Unexpected ET rates, nicely supported by ^1H NMR, IR, and MD results, show that there is a critical length marking the transition between short ligands, which form a fluid monolayer structure of folded chains, and longer alkyl chains, which self-organize into bundles. These results thus provide a different scenario for how an ultrasmall gold core talks with the surroundings through/with its monolayer. They also highlight the importance of ET rulers to shed light onto the solution structure of such elusive SAMs. We expect the outcome of this study to be useful for understanding, for example, the ET behavior of MPC layers in devices, the performances of MPCs in redox catalysis, and the interaction of these monolayers with complex environments such as cell membranes.

EXPERIMENTAL SECTION

MALDI-TOF Mass Spectrometry. MALDI-TOF experiments were carried out with an Applied Biosystems 4800 MALDI-TOF/TOF spectrometer equipped with a Nd:YAG laser operating at 355 nm. The laser firing rate was 200 Hz, and the accelerating voltage was 25 kV. *trans*-2-[3-(4-*tert*-Butylphenyl)-2-methyl-2-propenylidene] malononitrile (DCTB) was used as the matrix. The MPCs were dissolved in benzene containing DCTB to obtain 0.1 mM solutions with a 1:400 MPC/matrix ratio. Two microliters of solution were drop-casted onto the sample plate and air-dried. The spectra were recorded in the reflectron negative mode. As the standard, we used $Au_{25}(SC_2H_4Ph)_{18}$, which has a MW of 7394.

UV–Vis Absorption Spectroscopy. The UV–vis spectra of the MPCs were obtained at 0.1 mM concentration in DCM, with 2 mm cuvettes. The spectra resolution was 1 nm.

Infrared Absorption Spectroscopy. FT-IR absorption spectra were recorded in benzene solution using 1 mm optical path cells, CaF_2 windows, 1–2 mg mL^{-1} MPC concentrations, and an argon-flushed ThermoFisher Scientific Nicolet 6700 FT-IR spectrometer. The nominal resolution was 1 cm^{-1}, and 16 scans were averaged.

NMR Spectroscopy. ^1H NMR spectra were obtained at ~1 mM MPC concentration in C_6D_6 with a Bruker Avance DMX-600 MHz spectrometer equipped with a 5 mm TX-1 *x,y,z*-gradient powered, triple-resonance inverse probe operating at 599.90 MHz. The temperature was controlled (25 ± 0.1 °C, unless otherwise indicated) with a Bruker BVT-300 automatic temperature controller. Chemical shifts are in parts per million (δ units) with reference to tetramethylsilane used as an internal standard. To ensure a complete relaxation for all the resonances, integral values for the proton spectra were obtained by a prescan delay of 10 s. The proton assignments were performed by standard chemical shift correlations as well as by 2D correlation spectroscopy (COSY), total correlation spectroscopy (TOCSY), and nuclear Overhauser enhancement spectroscopy (NOESY) experiments, as previously done for $Au_{25}(SC_2H_4Ph)_{18}$.[28]

Electrochemistry. The working electrode was a 0.55 mm radius glassy carbon disk prepared, stored, and activated *in situ* according to a procedure ensuring formation of a reproducible surface suitable for ET studies.[42] A Pt wire was the counter electrode, and a Ag wire served as the quasi-reference electrode. At the end of each experiment, the potential of the latter was calibrated against the ferricenium/ferrocene redox couple (in DCM/0.1 M TBAH, $E^0 = 0.460$ V against the KCl saturated calomel electrode, SCE). The experiments were conducted in DCM/0.1 M TBAH under an Ar atmosphere in a glass cell thermostatted at 25 °C. For the electrode kinetics experiments, we used an EG&G-PARC 173/179 potentiostat digital coulometer, an EG&G-PARC 175 universal programmer, and a Nicolet 3091 12-bit resolution digital oscilloscope. To optimize the kinetic analysis, we used all experimental precautions and checks described in detail elsewhere.[19,29] To minimize the ohmic drop between the working and the reference electrodes, careful feedback correction was applied. The electrode kinetics experiments were also checked with a CHI 760d electrochemical workstation, which employs a different approach to perform feedback correction. The CV analysis was carried out on digital CV curves. For digital simulation, we used the DigiSim 3.03 package, using step size = 1 mV and exponential expansion factor = 0.5.

Molecular Dynamics Calculations. MD simulations were performed using the LAMMPS software.[43] Energy minimization was performed by using the steepest descent and then the conjugated gradient algorithm. This was followed by 1 ns in the microcanonical ensemble (NVE: fixed numbers of atoms *N*, volume *V*, and energy *E*), during which the temperature was taken to 300 K, and 1 ns in the isobaric–isothermal ensemble (NPT), with $T = 300$ K and $P = 1$ atm. Two nanoseconds were then run in the canonical ensemble (NVT), and the analysis was performed. Three-dimensional periodic boundary conditions were adopted. The Nosé–Hoover approach was used for the temperature and pressure control, with a dumping parameter of 100 and 1000 fs, respectively. The equations of motion were integrated using the velocity Verlet algorithm with a time step of 1 fs for the NVE and NPT simulations and of 2 fs for the NVT runs. Snapshots were taken every 1000 time steps. The cutoff for Lennard-Jones (LJ) interactions and the real-space part of the electrostatic potential was set to 12 Å. Electrostatic interactions were calculated using the particle–particle particle-mesh solver technique, with a root-mean-square accuracy of 10^{-4}. The bond lengths involving H atoms were constrained using the SHAKE algorithm. The all-atom CHARMM27 force field[44] was used for thiol chains and benzene. The gold atoms were allowed to interact with the chains and solvent *via* LJ potentials parametrized for the metal according to the universal force field (UFF).[45]

LJ cross-term interaction parameters were calculated according to the Lorentz−Berthelot combination rule. Au−Au, Au−S, and S−S interactions were set to zero. For Au and S atoms, we used the atomic coordinates of the X-ray structure of $Au_{25}(SC_2H_4Ph)_{18}$,[8] which were kept constant.

For the inertia tensor **I**, we used the following expression:

$$\mathbf{I} = \left\langle \sum_{i=1}^{\substack{\text{number}\\ \text{of ligands}}} \begin{pmatrix} m_C\left(y_i^2+z_i^2\right) & -m_C x_i y_i & -m_C x_i z_i \\ -m_C x_i y_i & m_C\left(x_i^2+z_i^2\right) & -m_C y_i z_i \\ -m_C x_i z_i & -m_C y_i z_i & m_C\left(x_i^2+y_i^2\right) \end{pmatrix} \right\rangle$$

where only the atomic coordinates x, y, and z of the nth carbon atoms, of mass m_C, along the thiol chains of $Au_{25}(SCn)_{18}$ were considered. Angular brackets indicate average over the simulation time. The dependence of the three components on n is illustrated in Figure S6. The semiaxes a, b, and c were obtained from the diagonalized tensor $\tilde{\mathbf{I}}$, in which M is the total mass:

$$\tilde{\mathbf{I}} = \begin{pmatrix} \tilde{I}^a & 0 & 0 \\ 0 & \tilde{I}^b & 0 \\ 0 & 0 & \tilde{I}^c \end{pmatrix} = \begin{pmatrix} M\left(b^2+c^2\right)/3 & 0 & 0 \\ 0 & M\left(a^2+c^2\right)/3 & 0 \\ 0 & 0 & M\left(a^2+b^2\right)/3 \end{pmatrix}$$

Conflict of Interest: The authors declare no competing financial interest.

Acknowledgment. This work was financially supported by the Ministry of University and Research (PRIN 20098Z4M5E), the University of Padova (PRAT CPDA103389), and AIRC (Project 12214: Innovative Tools for Cancer Risk Assessment and Early Diagnosis − 5 per mille).

Supporting Information Available: MPC synthesis and further NMR, IR, and MD figures. This material is available free of charge *via* the Internet at http://pubs.acs.org.

REFERENCES AND NOTES

1. Parker, J. F.; Fields-Zinna, C. A.; Murray, R. W. The Story of a Monodisperse Gold Nanoparticle: $Au_{25}L_{18}$. *Acc. Chem. Res.* **2010**, *43*, 1289–1296.
2. Murray, R. W. Nanoelectrochemistry: Metal Nanoparticles, Nanoelectrodes, and Nanopores. *Chem. Rev.* **2008**, *108*, 2688–2720.
3. Tsukuda, T. Toward an Atomic-Level Understanding of Size-Specific Properties of Protected and Stabilized Gold Clusters. *Bull. Chem. Soc. Jpn.* **2012**, *85*, 151–168.
4. Saha, K.; Agasti, S. S.; Kim, C.; Li, X.; Rotello, V. M. Gold Nanoparticles in Chemical and Biological Sensing. *Chem. Rev.* **2012**, *112*, 2739–2779.
5. Li, G.; Jin, R. Atomically Precise Gold Nanoclusters as New Model Catalysts. *Acc. Chem. Res.* **2013**, *46*, 1749–1758.
6. Heaven, M. W.; Dass, A.; White, P. S.; Holt, K. M.; Murray, R. W. Crystal Structure of the Gold Nanoparticle $[N(C_8H_{17})_4][Au_{25}(SCH_2CH_2Ph)_{18}]$. *J. Am. Chem. Soc.* **2008**, *130*, 3754–3755.
7. Zhu, M.; Aikens, C. M.; Hollander, F. J.; Schatz, G. C.; Jin, R. Correlating the Crystal Structure of a Thiol-Protected Au_{25} Cluster and Optical Properties. *J. Am. Chem. Soc.* **2008**, *130*, 5883–5885.
8. Zhu, M.; Eckenhoff, W. T.; Pintauer, T.; Jin, R. Conversion of Anionic $[Au_{25}(SCH_2CH_2Ph)_{18}]^-$ Cluster to Charge Neutral Cluster *via* Air Oxidation. *J. Phys. Chem. C* **2008**, *112*, 14221–14224.
9. Jadzinsky, P. D.; Calero, G.; Ackerson, C. J.; Bushnell, D. A.; Kornberg, R. D. Structure of a Thiol Monolayer-Protected Gold Nanoparticle at 1.1 Å Resolution. *Science* **2007**, *318*, 430–433.
10. Qian, H.; Eckenhoff, W. T.; Zhu, Y.; Pintauer, T.; Jin, R. Total Structure Determination of Thiolate-Protected Au_{38} Nanoparticles. *J. Am. Chem. Soc.* **2010**, *132*, 8280–8281.
11. Zeng, C.; Qian, H.; Li, T.; Li, G.; Rosi, N. L.; Yoon, B.; Barnett, R. N.; Whetten, R. L.; Landman, U.; Jin, R. Total Structure and Electronic Properties of the Gold Nanocrystal $Au_{36}(SR)_{24}$. *Angew. Chem., Int. Ed.* **2012**, *51*, 13114–13118.
12. Zeng, C.; Li, T.; Das, A.; Rosi, N. L.; Jin, R. Chiral Structure of Thiolate-Protected 28-Gold-Atom Nanocluster Determined by X-ray Crystallography. *J. Am. Chem. Soc.* **2013**, *135*, 10011–10013.
13. Cossaro, A.; Mazzarello, R.; Rousseau, R.; Casalis, L.; Verdini, A.; Kohlmeyer, A.; Floreano, L.; Scandolo, S.; Morgante, A.; Klein, M. L.; *et al.* X-ray Diffraction and Computation Yield the Structure of Alkanethiols on Gold(111). *Science* **2008**, *321*, 943–946.
14. Pensa, E.; Cortéz, E.; Corthey, G.; Carro, P.; Vericat, C.; Fonticelli, M. H.; Benitez, G.; Rubert, A. A.; Salvarezza, R. C. The Chemistry of the Sulfur−Gold Interface: In Search of a Unified Model. *Acc. Chem. Res.* **2012**, *45*, 1183–1192.
15. Häkkinen, H. The Gold−Sulfur Interface at the Nanoscale. *Nat. Chem.* **2012**, *4*, 443–455.
16. Love, J. C.; Estroff, L. A.; Kriebel, J. K.; Nuzzo, R. G.; Whitesides, G. M. Self-Assembled Monolayers of Thiolates on Metals as a Form of Nanotechnology. *Chem. Rev.* **2005**, *105*, 1103–1169.
17. Adams, D. M.; Brus, L.; Chidsey, C. E. D.; Creager, S.; Creutz, C.; Kagan, C. R.; Kamat, P. V.; Lieberman, M.; Lindsay, S.; Marcus, R. A.; *et al.* Charge Transfer on the Nanoscale: Current Status. *J. Phys. Chem. B* **2003**, *107*, 6668–6697.
18. Lee, D.; Donkers, R. L.; Wang, G.; Harper, A. S.; Murray, R. W. Electrochemistry and Optical Absorbance and Luminescence of Molecule-like Au_{38} Nanoparticles. *J. Am. Chem. Soc.* **2004**, *126*, 6193–6199.
19. Antonello, S.; Holm, A. H.; Instuli, E.; Maran, F. Molecular Electron-Transfer Properties of Au_{38} Clusters. *J. Am. Chem. Soc.* **2007**, *129*, 9836–9837.
20. Badia, A.; Lennox, R. B.; Reven, L. A Dynamic View of Self-Assembled Monolayers. *Acc. Chem. Res.* **2000**, *33*, 475–481.
21. Templeton, A. C.; Wuelfing, W. P.; Murray, R. W. Monolayer-Protected Cluster Molecules. *Acc. Chem. Res.* **2000**, *33*, 127–136.
22. Schaaff, T. G.; Shafigullin, M. N.; Khoury, J. T.; Vezmar, I.; Whetten, R. L. Properties of a Ubiquitous 29 kDa Au:SR Cluster Compound. *J. Phys. Chem. B* **2001**, *105*, 8785–8796.
23. Landman, U.; Luedtke, W. D. Structure, Dynamics, and Thermodynamics of Passivated Gold Nanocrystallites and Their Assemblies. *J. Phys. Chem.* **1996**, *100*, 13323–13329.
24. Landman, U.; Luedtke, W. D. Structure and Thermodynamics of Self-Assembled Monolayers on Gold Nanocrystallites. *J. Phys. Chem. B* **1998**, *102*, 6566–6572.
25. Negishi, Y.; Nobusada, K.; Tsukuda, T. Glutathione-Protected Gold Clusters Revisited: Bridging the Gap between Gold(I)−Thiolate Complexes and Thiolate-Protected Gold Nanocrystals. *J. Am. Chem. Soc.* **2005**, *127*, 5261–5270.
26. Tracy, J. B.; Kalyuzhny, G.; Crowe, M. C.; Balasubramanian, R.; Choi, J.-P.; Murray, R. W. Poly(ethylene glycol) Ligands for High-Resolution Nanoparticle Mass Spectrometry. *J. Am. Chem. Soc.* **2007**, *129*, 6706–6707.
27. Zhu, M.; Aikens, C. M.; Hendrich, M. P.; Gupta, R.; Qian, H.; Schatz, G. C.; Jin, R. Reversible Switching of Magnetism in Thiolate-Protected Au_{25} Superatoms. *J. Am. Chem. Soc.* **2009**, *131*, 2490–2492.
28. Venzo, A.; Antonello, S.; Gascón, J. A.; Guryanov, I.; Leapman, R. D.; Perera, N. V.; Sousa, A.; Zamuner, M.; Zanella, A.; Maran, F. Effect of the Charge State ($z = -1, 0, +1$) on the Nuclear Magnetic Resonance of Monodisperse $Au_{25}[S(CH_2)_2Ph]_{18}^z$ Clusters. *Anal. Chem.* **2011**, *83*, 6355–6362.
29. Antonello, S.; Perera, N. V.; Ruzzi, M.; Gascón, J. A.; Maran, F. Interplay of Charge State, Lability, and Magnetism in the Molecule-like $Au_{25}(SR)_{18}$ Cluster. *J. Am. Chem. Soc.* **2013**, *135*, 15585–15594.

30. Gray, H. B.; Winkler, J. R. Long-Range Electron Transfer. *Proc. Natl. Acad. Sci. U.S.A.* **2005**, *102*, 3534–3539.
31. Berlin, Y. A.; Grozema, F. C.; Siebbeles, L. D. A.; Ratner, M. A. Charge Transfer in Donor−Bridge−Acceptor Systems: Static Disorder, Dynamic Fluctuations, and Complex Kinetics. *J. Phys. Chem. C* **2008**, *112*, 10988–11000.
32. Antonello, S.; Hesari, M.; Polo, F.; Maran, F. Electron Transfer Catalysis with Monolayer Protected Au_{25} Clusters. *Nanoscale* **2012**, *4*, 5333–5342.
33. Holmlin, R. E.; Ismagilov, R. F.; Haag, R.; Mujica, V.; Ratner, M. A.; Rampi, M. A.; Whitesides, G. M. Correlating Electron Transport and Molecular Structure in Organic Thin Films. *Angew. Chem., Int. Ed.* **2001**, *40*, 2316–2320.
34. Paddon-Row, M. N. Superexchange-Mediated Charge Separation and Charge Recombination in Covalently-Linked Donor−Bridge−Acceptor Systems. *Aus. J. Chem.* **2003**, *56*, 729–748.
35. Dass, A.; Stevenson, A.; Dubay, G. R.; Tracy, J. B.; Murray, R. W. Nanoparticle MALDI-TOF Mass Spectrometry without Fragmentation: $Au_{25}(SCH_2CH_2Ph)_{18}$ and Mixed Monolayer $Au_{25}(SCH_2CH_2Ph)_{18-x}(L)_x$. *J. Am. Chem. Soc.* **2008**, *130*, 5940–5946.
36. Gottlieb, H. E.; Kotlyar, V.; Nudelman, A. NMR Chemical Shifts of Common Laboratory Solvents as Trace Impurities. *J. Org. Chem.* **1997**, *62*, 7512–7515.
37. Porter, M. D.; Bright, T. B.; Allara, D. L.; Chidsey, C. E. D. Spontaneously Organized Molecular Assemblies. 4. Structural Characterization of *n*-Alkyl Thiol Monolayers on Gold by Optical Ellipsometry, Infrared Spectroscopy, and Electrochemistry. *J. Am. Chem. Soc.* **1987**, *109*, 3559–3568.
38. Hostetler, M. J.; Stokes, J. J.; Murray, R. W. Infrared Spectroscopy of Three-Dimensional Self-Assembled Monolayers: *N*-Alkanethiolate Monolayers on Gold Cluster Compounds. *Langmuir* **1996**, *12*, 3604–3612.
39. Nicholson, R. S. Theory and Application of Cyclic Voltammetry for Measurement of Electrode Reaction Kinetics. *Anal. Chem.* **1965**, *37*, 1351–1355.
40. Peterson, R. R.; Cliffel, D. E. Scanning Electrochemical Microscopy Determination of Organic Soluble MPC Electron-Transfer Rates. *Langmuir* **2006**, *22*, 10307–10314.
41. Antonello, S.; Crisma, M.; Formaggio, F.; Moretto, A.; Taddei, F.; Toniolo, C.; Maran, F. Insights into the Free Energy Dependence of Intramolecular Dissociative Electron Transfers. *J. Am. Chem. Soc.* **2002**, *124*, 11503–11513.
42. Meneses, A. B.; Antonello, S.; Arévalo, M.-C.; Maran, F. Double-Layer Correction for Electron-Transfer Kinetics at Glassy Carbon and Mercury Electrodes in *N*,*N*-Dimethylformamide. *Electroanalysis* **2006**, *18*, 363–370.
43. Plimpton, S. Fast Parallel Algorithms for Short-Range Molecular Dynamics. *J. Comput. Phys.* **1995**, *117*, 1–19.
44. MacKerell, A. D., Jr.; Banavali, N.; Foloppe, N. Development and Current Status of the CHARMM Force Field for Nucleic Acids. *Biopolymers* **2000**, *56*, 257–265.
45. Rappé, A. K.; Casewit, C. J.; Colwell, K. S.; Goddard, W. A., III; Skiff, W. M. UFF, a Full Periodic Table Force Field for Molecular Mechanics and Molecular Dynamics Simulations. *J. Am. Chem. Soc.* **1992**, *114*, 10024–10035.